Synchronized Optical and Electronic Detection of Biomolecules Using a Low Noise Nanopore Platform

William H. Pitchford,[†,#] Hyung-Jun Kim,[‡,#] Aleksandar P. Ivanov,[†] Hyun-Mi Kim,[‡] Jae-Seok Yu,[‡] Robin J. Leatherbarrow,[†] Tim Albrecht,[*,†] Ki-Bum Kim,[*,‡] and Joshua B. Edel[*,†]

[†]Department of Chemistry, Imperial College London, South Kensington Campus, London SW7 2AZ, U.K. and [‡]Department of Materials Science and Engineering, Seoul National University, Seoul 151-742, Korea. [#]These authors (W.H.P. and H.-J.K.) contributed equally.

ABSTRACT In the past two decades there has been a tremendous amount of research into the use of nanopores as single molecule sensors, which has been inspired by the Coulter counter and molecular transport across biological pores. Recently, the desire to increase structural resolution and analytical throughput has led to the integration of additional detection methods such as fluorescence spectroscopy. For structural information to be probed electronically high bandwidth measurements are crucial due to the high translocation velocity of molecules. The most commonly used

solid-state nanopore sensors consist of a silicon nitride membrane and bulk silicon substrate. Unfortunately, the photoinduced noise associated with illumination of these platforms limits their applicability to high-bandwidth, high-laser-power synchronized optical and electronic measurements. Here we present a unique low-noise nanopore platform, composed of a predominately Pyrex substrate and silicon nitride membrane, for synchronized optical and electronic detection of biomolecules. Proof of principle experiments are conducted showing that the Pyrex substrates have substantially lowers ionic current noise arising from both laser illumination and platform capacitance. Furthermore, using confocal microscopy and a partially metallic pore we demonstrate high signal-to-noise synchronized optical and electronic detection of dsDNA.
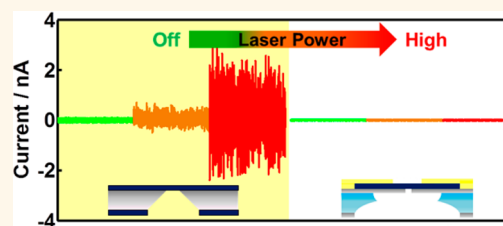
KEYWORDS: nanopore · single-molecule · fluorescence · noise · zero-mode waveguide

Initially inspired by molecular transport across biological pores and the Coulter counter, the use of nanopores as single molecule sensors has come into prominence in the past two decades with a remarkable quantity of research having been published.[1] The most commonly used detection method is that of resistive pulse sensing, where analyte molecules are electrophoretically driven across an insulating membrane, separating two sides of an electrolyte, *via* a nanopore. Single-molecule detection is subsequently provided by the transient reduction in pore conductance from the steady-state while an analyte is present in the pore. Using this technique, a wide range of analytes have now been studied, most commonly single- and double-stranded DNA and proteins, with both biological and solid-state nanopores.[2−5]

Recently, the desire to acquire complementary information, increase structural resolution and analytical throughput has led to the integration of additional detection methods such as transverse electrodes and optical detection *via* Raman and fluorescence spectroscopy.[6−9] The integration of fluorescence spectroscopy is of particular value due to its versatility: a range of molecular properties can be probed including molecular distance (*via* FRET), orientation (*via* polarization), and local environment (*via* quenching).[10] In addition, the nanopore platform provides the potential to enhance optical detection *via* control of throughput, incorporation of additional photonic structure or use as a zero-mode waveguide (ZMW).[7,11] A number of optical configurations have so far been reported, these include the use of wide-field imaging,[7] liquid core antiresonant reflecting optical waveguides,[12] total internal reflection fluorescence microscopy[13,14] and confocal fluorescence microscopy.[7]

For structural information to be probed *via* resistive pulse sensing, high temporal resolution measurements are crucial due to the high translocation velocity of molecules.

The most commonly used solid-state nanopore sensors consist of a silicon nitride membrane and bulk silicon substrate.[15] Unfortunately, the high frequency noise, so-called dielectric and input capacitance noise, associated with these platforms' high capacitance reduces the signal bandwidth at which molecules may be detected. Although integrated measurement electronics and additional dielectric layers can reduce background noise consequently increasing operating signal bandwidth,[16,17] an additional noise source exists under laser illumination due to the presence of Si.[18] This photoinduced noise significantly limits the applicability of these platforms to high-bandwidth, high-laser-power simultaneous optical and electronic measurements.

Here we present a unique low noise nanopore platform, composed of a predominately pyrex substrate and silicon nitride membrane as a platform for the synchronized optical and electronic detection of biomolecules.[19,20] Pyrex's high resistivity lowers device capacitance ($\sim$5$-$10 pF in 1 M KCl buffer) and therefore high frequency noise enabling sub-5 pA root mean square (RMS) ionic current measurements at 10 kHz bandwidth. Furthermore, the absence of a bulk Si substrate means photoinduced increases of RMS current are typically sub-pA in magnitude.

The application of a confocal microscope to a hybrid nanopore-zero mode waveguide platform is perhaps the most powerful technique for directly probing a single nanopore due to localized excitation volumes on the order of a zeptoliter and single photon resolution.[7,21] For this technique, a partially metallic nanopore is crucial so that no propagation modes for incident light exist within the nanopore. Using platforms coated with aluminum, we demonstrate synchronized optical and electronic detection of biomolecule translocation events. Aluminum was chosen due to its high extinction coefficient and high reflectivity at the desired wavelength (488 nm).[22] This enabled the use of membranes composed of only 30 nm thick aluminum and 20 nm

thick silicon nitride, therefore providing a small nanopore volume while also ensuring low transmittance of light across the pore and bulk membrane. We show signal-to-noise ratios of up to 15.6 are possible for the optical detection of Yoyo-1 labeled 5 kbp DNA (7.5 base pairs to one dye molecule) within 0.1 M KCl at a temporal resolution of 0.5 ms.

RESULTS AND DISCUSSION

A unique low-noise nanopore platform was used in this study in order to mitigate photoinduced ionic current noise. This device is composed of a nanopore within a pyrex substrate-based SiN$_x$ (Py-SiN$_x$) platform (Figure 1A) instead of a typical Si-substrate based SiN$_x$ (Si-SiN$_x$) platform (Figure 1B). Both platform types were fabricated so that their photoinduced noise characteristics could be compared within a typical 0.1 M KCl electrolyte (Materials and Methods). The devices contained a 20 nm thick SiN$_x$ free-standing membrane (Py-SiN$_x$, 5 μm $\times$ 5 μm; Si-SiN$_x$, 50 μm $\times$ 50 μm) into which 5$-$30 nm diameter nanopores were milled using a JEOL 2010F transmission electron microscope.

Simultaneous optical and electrical measurements were enabled by mounting nanopore devices in an optical cell, using a coverslip as a base. This enabled illumination of the nanopore using a custom-built confocal microscope (Figure 1E, Materials and Methods).[23] Briefly, nanopores were illuminated using an optical configuration employing a 488 nm continuous-wave solid-state laser (Sapphire 488LP, Coherent) and a 60x water immersion objective (1.20 NA, UPLSAPO 60XW, UIS2, Olympus). Fluorescence emission was split into two bands, 500$-$580 nm and 640$-$800 nm, before detection by two avalanche photodiodes and logged via a DAQ card at 100 kHz. A transmembrane potential was applied to the nanopores using an A-M systems 2400 patch-clamp amplifier with Ag/AgCl electrodes. Unless otherwise stated the analogue signal was low-pass filtered at 10 kHz before digitization at 100 kHz. Synchronised optical and electrical data acquisition
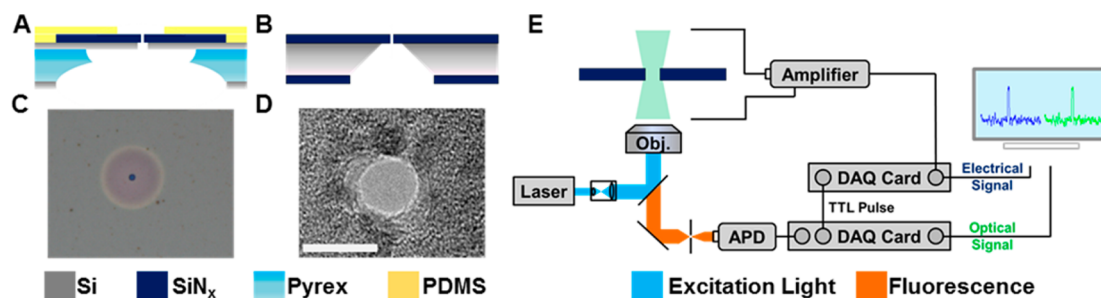

Figure 1. Schematics of (A) Pyrex and (B) Si substrate-based silicon nitride nanopore platforms. (C) Optical image of a Pyrex substrate (Py-SiN$_x$) platform (scale bar = 10 μm). Two circular features are present. The larger feature (diameter, $\sim$19 μm) corresponds to the aperture within the pyrex substrate and the smaller feature (diameter, $\sim$2.1 μm) to the free-standing silicon nitride membrane. (D) TEM image of a $\sim$7 nm diameter nanopore within the free-standing silicon nitride membrane of a Py-SiN$_x$ platform (scale bar = 10 nm). (E) The experimental setup: an epifluorescence optical configuration employing a 488 nm continuous-wave laser; a 60$\times$ water immersion objective (Obj.) and avalanche photodiode (APD) is used to probe a SiN$_x$ nanopore (Materials and Methods). When electrical data acquisition is initiated, a TTL pulse is generated by the electrical data acquisition (DAQ) card which subsequently triggers optical acquisition.
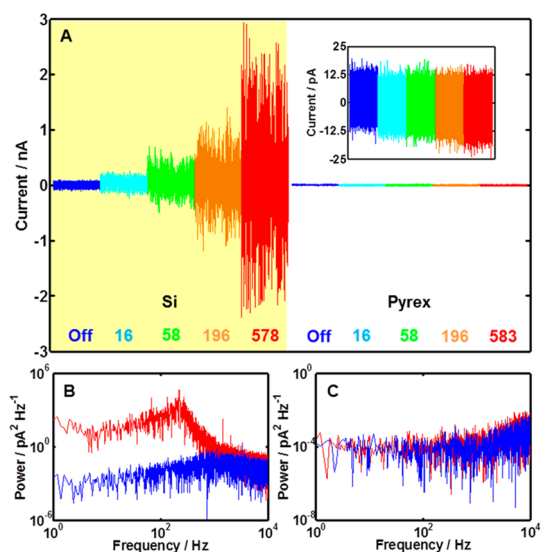
Figure 2. (A) Baseline ionic current at 0 mV, under laser illumination, for a ~27 nm diameter nanopore in a Si-SiN$_x$ (yellow background) and Py-SiN$_x$ platform. Different color traces correspond to different laser powers, as indicated by the number (in μW units) beneath each trace. The inset is an expanded view of data for the Py-SiN$_x$ device. (B) Power spectral densities at 0 mV for the Si-SiN$_x$ platform with the laser off (blue) and at ~578 μW laser power (red). (C) Power spectral densities at 0 mV for the Py-SiN$_x$ platform with the laser off (blue) and at ~583 μW laser power (red).

was enabled through the use of hardware and a custom LabView program for optical data acquisition (Figure 1E). Briefly, optical data acquisition using the Labview program was triggered by a TTL pulse, generated *via* a DAQ card once electrical data acquisition was initiated using Strathclyde Electrophysiology Software (WinWCP V4 8.4).

As a result of Pyrex's high resistivity (400 MΩ m), Py-SiN$_x$ platforms have lower capacitance (~5–10 pF in 1 M KCl buffer) and therefore exhibit lower dielectric and input capacitance noise than Si-SiN$_x$ platforms (boron doped, Si substrate resistivity: 1–30 Ω cm).[24] Consequently, with the laser turned off, the level of electrical noise for Py-SiN$_x$ platforms was lower than that for Si-SiN$_x$ platforms. For example, the standard deviation of ionic current at 0 mV bias, with the laser turned off, for a ~27 nm diameter nanopore was only 4.02 $\pm$ 0.02 pA for a Py-SiN$_x$ platform compared to 26.9 $\pm$ 0.9 pA for a Si-SiN$_x$ platform. Furthermore, bypassing the low pass Bessel filter integrated within the amplifier, a Py-SiN$_x$ platform provides a standard deviation of only 6.74 pA at 0 mV bias. As the dimensions of these pores are similar, they will exhibit comparable thermal noise.[24] Hence, the low noise exhibited by the Py-SiN$_x$ platform is a direct consequence of its low capacitance. There is also a substantial difference in the response of the devices to laser illumination. Figure 2A shows the baseline ionic current at 0 mV bias for a nanopore within a Py-SiN$_x$ and Si-SiN$_x$ platform, as laser power is raised to ~580 μW in magnitude. Assuming a cylindrical geometry, the pores have an

approximate diameter of 27 nm based on the measured pore conductance (Py-SiN$_x$ conductance, 25.5 nS; Si-SiN$_x$ conductance, 25.4 nS).[1] The standard deviation of the ionic current increases by 780.1 $\pm$ 25.8 pA (2864.2 $\pm$ 95.1%) for the Si-SiN$_x$ platform compared to only 0.9 $\pm$ 0.1 pA (17.6 $\pm$ 1.4%) for the Py-SiN$_x$ platform (Figure S1, Supporting Information). Figure 2 panels B and C show power spectrum densities (PSDs) for both platforms with the laser off and at ~580 μW laser power. Interestingly, a broad peak centered at ~225 Hz exists at ~580 μW laser power for the Si-SiN$_x$ platform. Both photoinduced heating of the electrolyte and surface charge change for silicon nitride nanopores have previously been reported.[25,26] However, the frequency dependence of this noise source is inconsistent with that of surface charge protonation noise or temperature-dependent thermal and dielectric noise.[24,27] Furthermore, this peaks absence within the Py-SiN$_x$ platforms power spectrum suggests the source of noise is related to the Si substrate. The optical transparency of the SiN$_x$ membrane and photon energy (2.54 eV) is sufficient for electron–hole pair generation in the Si substrate (band gap ~1.1 eV), reported to promote photoreduction of H$^+$ at p-type Si interfaces.[28] We therefore suspect, as previously reported, that the increase in noise is *via* electrochemical reaction at the silicon–electrolyte interface.[18]

The small increase of noise for Py-SiN$_x$ platforms stems from an increase in pore conductance with laser illumination and is a result of flicker noise scaling with the square of the ionic current and thermal noise being directly proportional to pore conductance.[24,29] Figure 3A shows current–voltage characteristics and corresponding conductance's at 0 mV bias for a ~7 nm diameter pore (conductance, 4.0 nS at 0 mV) at laser powers up to ~596 μW. Increases in noise for this nanopore are minor: sub-pA at 0 mV, 100 mV, and 200 mV bias across the entire laser power range (Figure 3B). The linear scaling of pore conductance with laser power may be a result of increases in pore surface charge and local heating of the electrolyte.[25,26] Previous studies suggest temperature change is likely to be small. For instance, the absorption coefficient of water for 488 nm wavelength light (0.0144 m^{-1}) is significantly lower than for 1064 nm wavelength light (12 m^{-1}) which has been reported to increase temperature at a rate of 20 K per mW.[26,30] Furthermore, introduction and translocation of 5 kbp DNA (0.75 nM), using this nanopore, revealed a reduction of translocation frequency by 25.8 $\pm$ 1.5% and 60.4 $\pm$ 5.6% at ~74 μW and ~204 μW laser power respectively (Figure S2, Supporting Information). An increase in surface charge is expected to reduce translocation frequency due to higher electro-osmotic flow, while the opposite trend is expected from local heating due to lower solution viscosity.[25,31−33] These findings
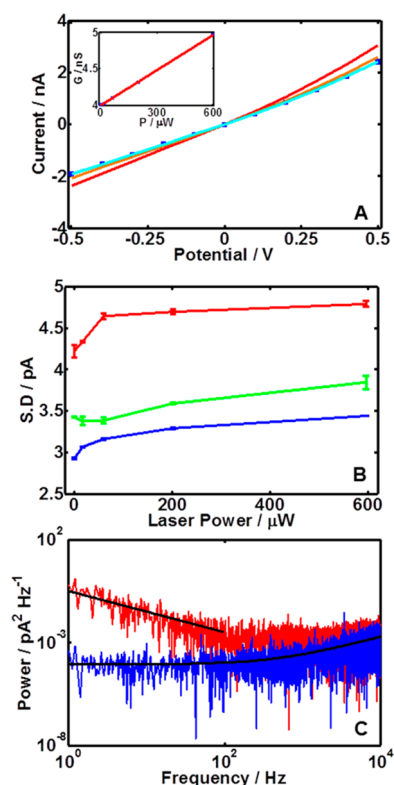
Figure 3. (A) Current–voltage trace for a ~7 nm diameter (conductance, 4.0 nS at 0 mV) Py-SiN$_x$ nanopore with the laser off (dark blue) and at ~17 μW (light blue), ~201 μW (orange), and ~596 μW (red) power. The inset shows pore conductance at 0 mV as a function of laser power. (B) Standard deviation of ionic current *versus* laser power with a bias of 0 mV (blue), −100 mV (green), and −200 mV (red). (C) Power spectral densities at 0 mV (blue) and −200 mV (red) with the laser power at ~596 μW. Black lines indicate fits of $S(f) = Af^{-a}$ and $S(f) = B + Cf + Df^2$ (where $A-D$ are fitting parameters and $0 < \alpha < 2$, with exponent α typically close to 1) for data collected at −200 mV and 0 mV, respectively.

suggest that increases in surface charge are the primary source of conductance change. By assuming changes in pore conductance were due to an increase in surface charge density alone, an expression which provided conductance as a function of laser power was derived and fit to the inset within Figure 3A (Supporting Information, eq 3). This expression provided an estimate of 27.9 mC m^{-2} for the surface charge density with the laser turned off and 20.0 C m^{-2} W^{-1} for the rate of change of surface charge. Both values are in good agreement with literature.[25,27]

PSDs of the ionic current at 200 mV and 0 mV bias were fit with $S_n(f) = Af^{-\alpha}$ and $S_n(f) = B + Cf + Df^2$, respectively, where f is frequency; A is the amplitude of flicker noise; B is the amplitude of white (thermal) noise; C is the amplitude of dielectric noise, and D is the amplitude of input capacitance noise (Figure 3C).[24,34] As expected, this analysis revealed an increase in the amplitude of both flicker noise and white (thermal) noise with laser power (Figure S3, Supporting Information). Owing to the dependence of the dielectric and input capacitance noise on frequency

($\propto F$ and $\propto F^2$, respectively), power spectrum analysis for these was conducted on ionic current data low-pass filtered at 20 kHz to increase the fitting range and certainty of the extracted parameters. No significant dependence of the amplitude of either dielectric or input capacitance noise on laser power was found (Figure S4, Supporting Information).

Increases in the amplitude of thermal noise (B) are in line with conductance changes as predicted using a thermal noise model, $B = 4k_BTG$, where T is temperature and G is pore conductance. For instance, at ~596 μW laser power the amplitude of thermal noise increased by 35.0 ± 9.1% and pore conductance increased by 25% (Figure 3a, inset). At ~596 μW laser power, the amplitude of flicker noise increased by 87.0 ± 45.4% (Figure S3, Supporting Information). The amplitude of flicker noise is known to scale with the square of the ionic current (*i.e.*, $A \propto I^2$).[24,35] The noise amplitude once normalized with respect to I^2 is approximately constant across the laser power range with a mean of $(3.56 \pm 0.17) \times 10^{-7}$ Hz^{-1} (Figure S3, inset, Supporting Information). This implies that the rise in amplitude of flicker noise occurs because of the increase in magnitude of the current.

Previous studies have shown that nanopores which exhibit low flicker noise (<1 pA^2/Hz at 1 Hz) may be described by Hooges relation, which characterizes flicker noise arising from fluctuations in bulk electrolyte mobility.[17] In such cases, the flicker noise amplitude (A) is given by $A = aI^2/f$, where I is current; f is frequency, and a is the normalized noise amplitude. The normalized noise amplitude is given by $a = \alpha/N_c$ where N_c is the number of charge carriers and α is the Hooge parameter.[35−37] Upon illumination of a nanopore, the surface charge density increases and hence so does the number of charge carriers. If the Hooge relation is obeyed, the normalized noise amplitude (a) would therefore decrease with laser power. The independence of the normalized flicker noise amplitude to laser power therefore suggests that mobility fluctuations are not the sole mechanism responsible for flicker noise in this system. A variety of additional flicker noise sources have been reported, including nanobubbles and inhomogeneous surface charge, which could be present simultaneously.[17,38,39]

For Si-SiN$_x$ platforms, the broad peak at ~225 Hz within PSDs, associated with photoinduced electrochemical reaction, prevented the same procedure of analysis. Nonetheless, visual inspection of Figure 2B shows a substantial increase in the amplitude of noise below 1000 Hz at ~578 μW laser power and 0 mV bias. Use of a smoothing spline indicated an increase in the amplitude of noise at 225 and 1 Hz by factors of $(1.79 \pm 0.17) \times 10^5$ and $(7.74 \pm 2.56) \times 10^4$, respectively. These noise characteristics are in stark contrast to Py-SiN$_x$ devices. For comparative purposes, the same analysis was conducted on Figure 2C as it was collected with a

similar sized (∼27 nm diameter) Py-SiN$_x$ nanopore. Here, illumination with ∼583 μW laser power induced an increase by a factor of only 1.48 ± 0.05 and 1.49 ± 0.06 at 1 and 225 Hz, respectively. Figure S5 within the Supporting Information contains PSDs for both devices, normalized with respect to I^2, at −200 mV bias with the laser turned off and on. For this Si-SiN$_x$ nanopore, at ∼578 μW laser power the magnitude and breadth of the peak at ∼225 Hz is great enough to obscure flicker noise. Whereas for the Py-SiN$_x$ platform, as previously discussed, increases of low frequency noise are in accordance with the growth of flicker noise associated with higher ionic current. Comparison of these PSDs highlights the significance of the additional source of noise for Si-SiN$_x$ platforms. In addition, it shows the distinct improvement that a predominately pyrex substrate provides: ionic current measurements at a noise floor defined by the magnitude of conductance change induced by laser illumination.

Synchronized Detection. The low-light induced noise of Py-SiN$_x$ nanopore devices makes them ideal for utilization with confocal microscopy for synchronized optical and electronic detection of biomolecules. Previous studies have demonstrated the advantages of a hybrid nanopore-zero-mode waveguide platform: reduced background photon noise, the ability to precisely localize a molecule within the optical probe volume and control of throughput.[7,40] This powerful technique involves illumination of a partially metallic nanopore where, crucially, the lateral dimensions of the nanopore mean no propagation modes exist for the incident light. As a result, light inside the aperture decays evanescently resulting in confined excitation volumes on the order of a zeptoliter (1 × 10^{-21}). It is important that pore length is not increased substantially by a metallic layer, as changes in pore conductance induced by a translocating molecule are inversely proportional to pore length.[41] Thus, Py-SiN$_x$ platforms were coated with 30 nm thick aluminum using electron beam evaporation before milling of a sub-30 nm diameter pore. This structure was selected as it provided a small nanopore volume while also ensuring low transmittance of light across the pore and bulk membrane. Transmittance of light across the bulk membrane is significantly attenuated, with a reduction in the electromagnetic field intensity across a 30 nm thick Al membrane of ∼20 dB (10 log$_{10}$|**E**|^2).[22] Furthermore, at the wavelength of interest (488 nm), the ZMW cutoff diameter is 215 nm ensuring attenuation of light intensity along the pore-axis.[22] Assuming the ZMW was fabricated using a perfect conductor, the intensity of light decays according to the below expression where h is pore depth, I_h is intensity at depth h, I_o is initial intensity, λ_c is the cutoff wavelength and λ_m is the wavelength of incident light.[42] Using this equation, a reduction of intensity by 99.6% is expected at a depth of 5 nm within a 10 nm diameter pore. It should be

noted that this only an estimate as attenuation is lower for real metals, owing to a finite skin depth.[43]

$$\frac{I_h}{I_o} = \exp\left(-\frac{4\pi h}{\lambda_b}\sqrt{\left(\frac{\lambda_m}{\lambda_c}\right)^2 - 1}\right)$$

Before attempting synchronized detection, independent optical and electronic measurements of the translocation of 5 kbp DNA were conducted to assess the viability of this platform for single molecule detection. Excellent signal-to-noise for both electronic and optical signals was provided by these nanopore platforms. Figure 4A shows a typical ionic current trace for a ∼19 nm diameter nanopore (conductance, 49.6 nS) within a 1 M KCl electrolyte, after introduction of 5 kbp DNA (2.6 nM) and application of a 100 mV bias. Corresponding event durations and amplitudes were extracted and are shown by a contour plot in Figure 4B. Translocation events of linear and folded DNA molecules are easily distinguished and are labeled as type 1 and 2 events, respectively.[3]

For optical detection, 5 kbp DNA was labeled with Yoyo-1 at ratio of 7.5 base pairs to one dye molecule. Yoyo-1 was selected because its absorbance maximum (491 nm) is close to the wavelength of the laser (488 nm). Figure 4C shows an example optical trace for 500−580 nm wavelength fluorescence at 300 mV bias and ∼17 μW laser power illumination, after the introduction of labeled DNA (0.85 nM) to a ∼13 nm diameter pore (conductance, 25.7 nS). The presence of a translocating DNA molecule within the optical probe volume results in a burst of fluorescence. Corresponding dwell times and event amplitudes were extracted, using a custom Matlab script, and are shown within a contour plot in Figure 4D. Signal-to-noise is excellent: the ratio of mean pulse height (28.5 ± 11.6 photons per 0.5 ms) to background photon counts (1.85 ± 0.65 photons per 0.5 ms) is 15.6 ± 8.3. The dwell time within the optical channel is larger than that would be expected in the electronic channel. A fit of a log-normal probability distribution function to a histogram of event duration provided a mean of 78.3 ± 3.9 ms. This is a result of a molecule which has left the nanopore being detected optically until it has left the focal plane *via* a combination of diffusion and electrokinetic phenomena.[7]

Synchronised optical and electrical data acquisition was enabled through the use of hardware and a custom LabView program for optical data acquisition (Figure 1B). The synchronization of optical and electrical signals was verified by illuminating a ∼14 nm diameter nanopore (conductance, 9.1 nS) with 1.87 mW laser power in finite intervals using an optical beam shutter (Thorlabs, SHO5). Photoinduced increases in pore conductance were correlated with an increase of background fluorescence from the pore surface, detected
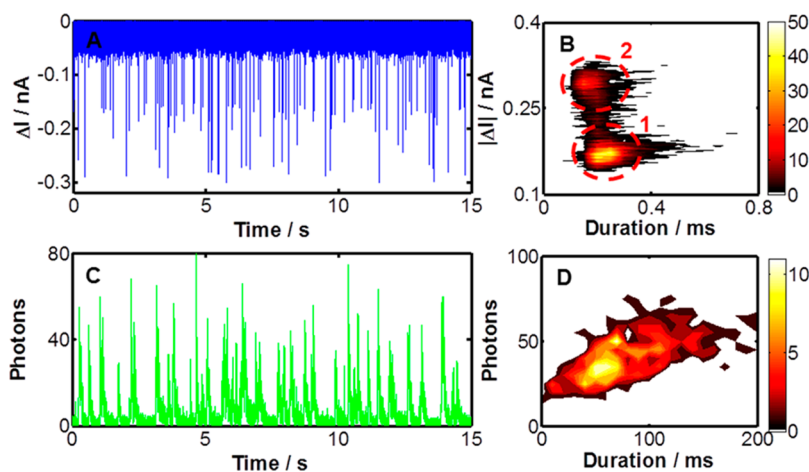
Figure 4. (A) Baseline-adjusted ionic current trace for electrical 5 kbp DNA translocation detection at 100 mV using a ~19 nm diameter pore (conductance: 49.6 nS) and 1 M KCl electrolyte. (B) Corresponding contour plot of event amplitude *versus* duration for 100 mV electrical detection data. (C) Photon trace (0.5 ms resolution) for optical Yoyo-1 labeled 5 kbp DNA (7.5 bp: 1 dye) translocation detection at 300 mV bias and ~17 μW laser power using a ~13 nm diameter pore (conductance: 25.7 nS) and 0.1 M KCl electrolyte. Data corresponds to 500−580 nm wavelength fluorescence. (D) Corresponding contour plot of event amplitude (photons per 0.5 ms) *versus* duration for 300 mV optical detection data.

within the red channel of the optical setup ($\lambda \approx$ 640−800 nm). Cross-correlation of the two signals was conducted, for a total of 14 pulses, to quantify any delay in acquisition. This indicated that the electronic signal trailed the optical signal by an average of 0.18 $\pm$ 0.02 ms (Figure S6, Supporting Information). This delay is close to the difference in rise-time of the two signals, 0.17 $\pm$ 0.08 ms, indicating that data acquisition was indeed synchronized.

To demonstrate synchronized detection, we introduced Yoyo-1 labeled 5 kbp DNA (0.790 nM) to a platform containing two pores (~10 nm and ~6 nm diameter, total conductance: 9.1 nS). Figure 5A shows a sample of the recorded ionic current ($I(t)$) and optical fluorescence ($F(t)$) signals at ~16 μW laser power and −400 mV applied bias. A total of 191 events were detected in the optical channel and 206 events in the electronic channel: a 92.7% synchronized detection efficiency. The slightly lower number of events in the optical channel is in part due to the longer dwell time of DNA within the optical detection volume (mean duration, 152.0 $\pm$ 23.0 ms, Figure 5D) resulting in amalgamation of consecutive translocation events. Accounting for such events provides an efficiency of 93.7%. Efficiency could be improved further by using an alternate fluorescent dye, for example Alexa Fluor 488 as its fluorescence is not quenched by halides, but this was deemed unnecessary for this proof of principle experiment.

Interestingly, an increase in ionic current upon exit of a DNA molecule from the pore is observed in 77.7% of events (160 events). This phenomenon was also observed for Py-SiN$_x$ platforms which contained a single nanopore, with and without Al (data not shown). Resistive pulses are a result of a decrease in the flux of ions across the pore and consequently pore conductance while a molecule is present. The mechanism responsible for a peak in ionic current (mean duration, 0.08 $\pm$ 0.03 ms; mean amplitude, 197.0 $\pm$ 37.9 pA) is less clear. If the diameter of the nanopore is close to that of dsDNA (2.2 nm) and its double layer ($\lambda_D = 0.97$ nm for 0.1 M KCl), this phenomenon can arise due to the release of accumulated electrolyte ions at the pore entrance after translocation and analyte double layer effects such as diffusive currents and concentration polarization.[44−46] However, the nanopore dimensions (~10 nm and ~6 nm) are larger than that of a single DNA molecule and hence these mechanisms are unlikely to be significant. Instead, we suspect this peak in ionic current arises from electrostatic enhancement of counterion concentration at the pore exit due to molecule surface charge.[47] Menestrina et al. have previously reported a decrease and subsequent increase in current upon entry and exit of negatively charged 470 nm diameter polystyrene particles across a 1400 nm diameter pore for electrolyte concentrations <300 mM KCl.[47] We believe that the peak in ionic current arises predominately due to this mechanism. We are not fully certain why this phenomenon is only observed in 77.7% of events, but this may be a consequence of differing conformations of DNA upon leaving the pore.

A histogram of resistive pulse height revealed a single cluster of events with a mean amplitude of 196.4 $\pm$ 67.8 pA (Figure 5C, inset). The corresponding molecule diameter was estimated, neglecting surface charge effects, using the expression derived by Smeets et al. as 4.57 $\pm$ 1.41 nm.[41] This indicates that molecules translocated predominantly in a folded conformation. A histogram of the resistive pulse duration, shown in Figure 5b, was fit with the 1D linear translocation probability density function reported by Ling et al.,
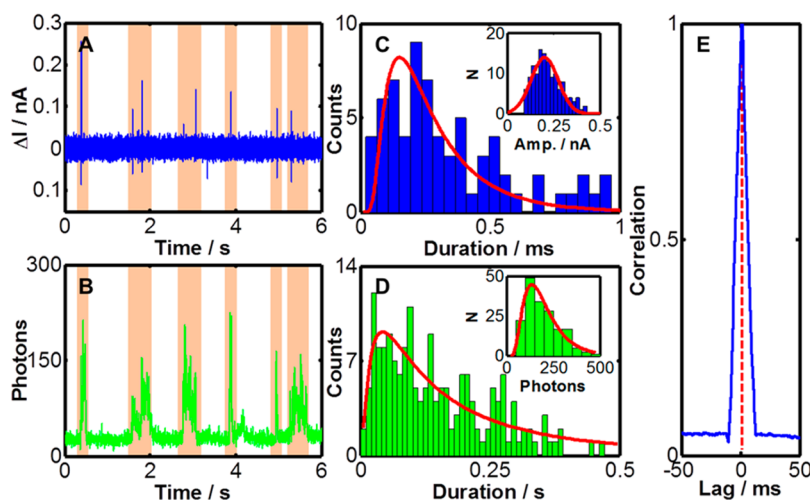
Figure 5. (A and B) Baseline adjusted ionic current and photon trace for Yoyo-1 labeled 5 kbp DNA (7.5 bp: 1 dye) translocation detection at 400 mV bias and ~17 μW laser power using two pores (~10 and 6 nm diameter; total conductance, 9.1 nS) and a 0.1 M KCl electrolyte. Data within the optical channel has been rebinned at 2 ms resolution. (C) Corresponding electrical data histograms of event duration and amplitude (inset) fit with Ling *et al*. and Gaussian probability distribution functions, respectively.[48] (D) Corresponding optical data histograms of event duration and amplitude (inset) fit with log-normal probability distribution functions. (E) Cross-correlation of the optical events within the green channel ($\lambda \approx 500-580$ nm) and the associated peaks in ionic current for the data set shown in panels A and B.

$F1(t) = (L/(4\pi Dt^3)1/2e^{-(L-vt)2/4Dt}$, where v is drift velocity, L is the length of 5 kbp dsDNA and D is the diffusion coefficient.[48] The length of unfolded 5 kbp DNA is 1.7 μm; the Ling distribution indicated a molecule length of 1.064 μm confirming that molecules were folded during translocation. The mean translocation time and drift velocity were 0.283 ms and 3.76 mm/s, which are in good agreement with the literature.[3,15]

Synchronization was verified measuring the cross-correlation of the optical and electrical signals. Owing to the irregular shape and long duration of optical events, they were replaced with pulses with the same duration as the corresponding electrical event. As a high proportion of electrical events were biphasic, the optical signal was cross-correlated with both resistive pulses and peaks in ionic current. Cross-correlation indicated that molecules were detected optically 80 μs after the resistive pulse and 109 μs before the peak in ionic current associated with exit from the pore. Figure 5E shows cross-correlation of the optical events and the associated peaks in ionic current for the data set shown in Figure 5A,B. The delay in optical detection with respect to the initial resistive pulse indicates that, due to the evanescent decay of incident light along the pore axes, the effective optical observation volume is indeed confined to the far region of the pore.

CONCLUSION

We have demonstrated synchronized optical and electronic detection of biomolecules using a unique low-noise nanopore platform. The presence of a Pyrex substrate substantially lowers ionic current noise arising from both laser illumination and platform

capacitance. Owing to the dependence of the dielectric and input capacitance noise on capacitance ($\propto C_{Chip}$ and $\propto C_{Chip}^2$, respectively[24]), an important advantage of the pyrex-based platforms is the low chip capacitance (5–10 pF in 1 M KCl). Typical Si substrate-based SiN$_x$ nanopore platforms have capacitances ranging from ~50 pF to ~370 pF.[36,49] As these noise sources dominate at bandwidths greater than 10 kHz, the improvements in the level of electrical noise exhibited by pyrex-based devices can therefore be expected to increase at higher bandwidths. This platform therefore provides scope for high-bandwidth and high-laser-power synchronized optical and electrical detection of biomolecules.

We foresee an array of potential applications of the platform, with or without the additional Al membrane, such as probing the translocation mechanism, enhanced conformational analysis (*e.g. via* single-particle FRET), label-free optical detection of biomolecules, and superior analyte discrimination within complex solutions.[50] Nevertheless, the use of a partially metallic pore as a zero-mode waveguide has distinct advantages: excellent optical signal-to-noise due to a reduction of background photon noise and the ability to precisely localize a molecule within the probe volume. Furthermore, functionality could be enhanced by incorporation of the appropriate photonic structure for control of local temperature, *via* plasmonic heating, and enable single molecule thermodynamic and kinetic biophysical studies.[33,51] For example, one can envisage experiments involving the modulation of temperature and subsequent probing of structural dynamics using electronic and optical detection. Ultimately, the application of these low-noise platforms to

synchronized optical and electronic detection enhances nanopore sensitivity and increases both the range of molecules which can be studied and potential applications of these sensors.

MATERIALS AND METHODS

Silicon substrate-based silicon nitride (Si-SiN$_x$) devices were fabricated from boron doped, ⟨100⟩ crystal orientation, 500 μm thick silicon wafers coated with 20 nm thick low-stress silicon nitride (SiN$_x$). Briefly, wafers were segmented *via* photolithography and reactive ion etching (RIE) into 10 mm × 10 mm chips, each with a central square window of SiN$_x$ removed. A wet KOH etch was subsequently used to establish a ~50 μm × 50 μm free-standing SiN$_x$ membrane before milling of a nanopore using a JEOL 2010F transmission electron microscope.

Pyrex substrate-based silicon nitride (Py-SiN$_x$) devices were fabricated as follows. Pyrex substrates (10 mm × 10 mm, 200 μm thick) were coated with amorphous Si (a-Si, 200 nm thick) on both sides *via* low pressure chemical vapor deposition. Photolithography and RIE were used to "open" a 5 μm × 5 μm window in *a*-Si on the topside of the wafer before a HF wet etch (49 wt %, 5 min) of the exposed pyrex. Photolithography and RIE were then used to define a 100 μm × 100 μm opening in *a*-Si on the bottom side of the wafer and a HF wet etch (49 wt %) of the exposed pyrex used to merge the two etched chambers. SiN$_x$ membranes (20 nm thick) were prepared separately *via* plasma-enhanced chemical vapor deposition onto a Ni–Si platform. Poly(methyl methacrylate) (PMMA, 200 nm thick) was then deposited *via* spin coating, yielding a PMMA/SiN$_x$/Ni/Si structure. Addition to a FeCl$_3$ solution dissolved the Ni present, establishing a PMMA/SiN$_x$ membrane which was added to the topside of the Py-SiN$_x$ platform. PMMA was subsequently dissolved using acetone, and the SiN$_x$ membrane was secured by depositing photo-definable PDMS (10–20 μm thick).[52] For synchronized detection using a zero-mode waveguide modality, a 30 nm thick aluminum layer was deposited onto the topside of the Py-SiN$_x$ platform (Py-SiN$_x$-Al) *via* electron beam evaporation before deposition of PDMS.

All experiments were conducted using a reported custom-built confocal microscope.[54,55] Nanopores were illuminated using a 488 nm continuous-wave solid-state laser (Sapphire 488LP, Coherent) and a 60× water immersion objective (1.20 NA, UPLSAPO 60XW, UIS2, Olympus). Fluorescence emission was split into two bands, 500–580 nm and 640–800 nm, using a dichroic mirror (630DCXR) before detection by two avalanche photodiodes (SPCM-AQR-14, PerkinElmer) coupled with a DAQ card (NI 6602, National Instruments) for data logging. A transmembrane potential was applied to nanopore sensors using an A-M systems 2400 patch-clamp amplifier and Ag/AgCl electrodes. Unless otherwise stated, the analogue signal was filtered by an integrated six-position, four-pole, low-pass Bessel filter at 10 kHz before digitization at 100 kHz using a NI-USB 6259 DAQ card. All electrolytes were buffered using 10 mM Tris.HCl, 1 mM EDTA (pH7).

Custom Matlab scripts were used for data analysis. Power spectra were estimated, using a fast-Fourier transform and 9.75 s duration data sets. To rectify signal attenuation before the cutoff frequency, power spectra were normalized by the magnitude response of a four-pole, low-pass Bessel filter at the corresponding low pass filter frequency.[16] RMS current was calculated using 0.2 s ionic current traces.

The peak selection criterion for both optical and electrical translocation data was a minimum amplitude of 5 standard deviations of the background signal. To account for ionic current noise, the baseline of all electrical data was smoothed using an asymmetric least-squares smoothing algorithm before peak selection.[53]

Conflict of Interest: The authors declare no competing financial interest.

REFERENCES AND NOTES

1. Wanunu, M. Nanopores: A Journey towards DNA Sequencing. *Phys. Life Rev.* **2012**, *9*, 125–158.
2. Fologea, D.; Gershow, M.; Ledden, B.; McNabb, D. S.; Golovchenko, J. A.; Li, J. Detecting Single Stranded DNA with a Solid State Nanopore. *Nano Lett.* **2005**, *5*, 1905–1909.
3. Storm, A. J.; Chen, J. H.; Zandbergen, H. W.; Dekker, C. Translocation of Double-Strand DNA through a Silicon Oxide Nanopore. *Phys. Rev. Stat. Nonlinear, Soft Matter Phys.* **2005**, *71*, 51903.
4. Fologea, D.; Ledden, B.; McNabb, D. S.; Li, J. L. Electrical Characterization of Protein Molecules by a Solid-State Nanopore. *Appl. Phys. Lett.* **2007**, *91*.
5. Bayley, H.; Cremer, P. S. Stochastic Sensors Inspired by Biology. *Nature* **2001**, *413*, 226–230.
6. Ivanov, A. P.; Instuli, E.; McGilvery, C. M.; Baldwin, G.; McComb, D. W.; Albrecht, T.; Edel, J. B. DNA Tunneling Detector Embedded in a Nanopore. *Nano Lett.* **2011**, *11*, 279–285.
7. Chansin, G. A. T.; Mulero, R.; Hong, J.; Kim, M. J.; deMello, A. J.; Edel, J. B. Single-Molecule Spectroscopy Using Nanoporous Membranes. *Nano Lett.* **2007**, *7*, 2901–2906.
8. Cecchini, M. P.; Wiener, A.; Turek, V. A.; Chon, H.; Lee, S.; Ivanov, A. P.; McComb, D. W.; Choo, J.; Albrecht, T.; Maier, S. A.; *et al.* Rapid Ultrasensitive Single Particle Surface-Enhanced Raman Spectroscopy Using Metallic Nanopores. *Nano Lett.* **2013**, *13*, 4602–4609.
9. Miles, B. N.; Ivanov, A. P.; Wilson, K. A.; Dogan, F.; Japrung, D.; Edel, J. B. Single Molecule Sensing with Solid-State Nanopores: Novel Materials Methods and Applications. *Chem. Soc. Rev.* **2013**, *42*, 15–28.
10. Deniz, A. a; Mukhopadhyay, S.; Lemke, E. a. Single-Molecule Biophysics: At the Interface of Biology, Physics and Chemistry. *J. R. Soc. Interface* **2008**, *5*, 15–45.
11. Aouani, H.; Mahboub, O.; Bonod, N.; Devaux, E.; Popov, E.; Rigneault, H.; Ebbesen, T. W.; Wenger, J. Bright Unidirectional Fluorescence Emission of Molecules in a Nanoaperture with Plasmonic Corrugations. *Nano Lett.* **2011**, *11*, 637–644.
12. Liu, S.; Zhao, Y.; Parks, J. W.; Deamer, D. W.; Hawkins, A. R.; Schmidt, H. Correlated Electrical and Optical Analysis of Single Nanoparticles and Biomolecules on a Nanopore-Gated Optofluidic Chip. *Nano Lett.* **2014**, *14*, 4816–4820.
13. Soni, G. V.; Singer, A.; Yu, Z.; Sun, Y.; McNally, B.; Meller, A. Synchronous Optical and Electrical Detection of Biomolecules Traversing through Solid-State Nanopores. *Rev. Sci. Instrum.* **2010**, *81*, 014301.
14. McNally, B.; Singer, A.; Yu, Z.; Sun, Y.; Weng, Z.; Meller, A. Optical Recognition of Converted DNA Nucleotides for Single-Molecule DNA Sequencing Using Nanopore Arrays. *Nano Lett.* **2010**, *10*, 2237–2244.
15. Li, J.; Gershow, M.; Stein, D.; Brandin, E.; Golovchenko, J. A. DNA Molecules and Configurations in a Solid-State Nanopore Microscope. *Nat. Mater.* **2003**, *2*, 611–615.
16. Rosenstein, J. K.; Wanunu, M.; Merchant, C. a; Drndic, M.; Shepard, K. L. Integrated Nanopore Sensing Platform with

Sub-Microsecond Temporal Resolution. *Nat. Methods* **2012**, *9*, 487–492.

17. Tabard-Cossa, V.; Trivedi, D.; Wiggin, M.; Jetha, N. N.; Marziali, A. Noise Analysis and Reduction in Solid-State Nanopores. *Nanotechnology* **2007**, *18*, 305505.

18. Li, Y.; Chen, C.; Kerman, S.; Neutens, P.; Lagae, L.; Groeseneken, G.; Stakenborg, T.; Van Dorpe, P. Harnessing Plasmon-Induced Ionic Noise in Metallic Nanopores. *Nano Lett.* **2013**, *13*, 1724–1729.

19. Huisman, E. M.; Biance, A.-L.; Madouri, A.; Patriarche, G.; Bourhis, E.; Oukhaled, G.; Auvray, L.; Gierak, J. A New Way to Integrate Solid State Nanopores for Translocation Experiments. *Microelectron. Eng.* **2008**, *85*, 1311–1313.

20. Lee, M.-H.; Kumar, A.; Park, K.-B.; Cho, S.-Y.; Kim, H.-M.; Lim, M.-C.; Kim, Y.-R.; Kim, K.-B. A Low-Noise Solid-State Nanopore Platform Based on a Highly Insulating Substrate. *Sci. Rep.* **2014**, *4*.

21. Larkin, J.; Foquet, M.; Turner, S. W.; Korlach, J.; Wanunu, M. Reversible Positioning of Single Molecules inside Zero-Mode Waveguides. *Nano Lett.* **2014**, *14*, 6023–6029.

22. Hong, J.; Lee, Y.; Chansin, G. A. T.; Edel, J. B.; deMello, A. J. Design of a Solid-State Nanopore-Based Platform for Single-Molecule Spectroscopy. *Nanotechnology* **2008**, *19*, 165205.

23. Huebner, A.; Srisa-Art, M.; Holt, D.; Abell, C.; Hollfelder, F.; DeMello, A. J.; Edel, J. B. Quantitative Detection of Protein Expression in Single Cells Using Droplet Microfluidics. *Chem. Commun.* **2007**, 1218–1220.

24. Tabard-Cossa, V. Instrumentation for Low-Noise High-Bandwidth Nanopore Recording. In *Engineered Nanopores for Bioanalytical Applications*; Edel, J. B., Albrecht, T., Eds.; Micro and Nano Technologies; William Andrew Publishing: Oxford, 2013; pp 59−93.

25. Di Fiori, N.; Squires, A.; Bar, D.; Gilboa, T.; Moustakas, T. D.; Meller, A. Optoelectronic Control of Surface Charge and Translocation Dynamics in Solid-State Nanopores. *Nat. Nanotechnol.* **2013**, *8*, 946–951.

26. Keyser, U. F.; Krapf, D.; Koeleman, B. N.; Smeets, R. M. M.; Dekker, N. H.; Dekker, C. Nanopore Tomography of a Laser Focus. *Nano Lett.* **2005**, *5*, 2253–2256.

27. Hoogerheide, D. P.; Garaj, S.; Golovchenko, J. A. Probing Surface Charge Fluctuations with Solid-State Nanopores. *Phys. Rev. Lett.* **2009**, *102*, 256804.

28. Mathews, N. R.; Sebastian, P. J.; Mathew, X.; Agarwal, V. Photoelectrochemical Characterization of Porous Si. *Int. J. Hydrogen Energy* **2003**, *28*, 629–632.

29. Chen, P.; Mitsui, T.; Farmer, D. B.; Golovchenko, J.; Gordon, R. G.; Branton, D. Atomic Layer Deposition to Fine-Tune the Surface Properties and Diameters of Fabricated Nanopores. *Nano Lett.* **2004**, *4*, 1333–1337.

30. Hale, G. M.; Querry, M. R. Optical Constants of Water in the 200-nm to 200-mm Wavelength Region. *Appl. Opt.* **1973**, *12*, 555–563.

31. Meller, A.; Nivon, L.; Brandin, E.; Golovchenko, J.; Branton, D. Rapid Nanopore Discrimination between Single Poly-nucleotide Molecules. *Proc. Natl. Acad. Sci. U.S.A.* **2000**, *97*, 1079–1084.

32. Fologea, D.; Uplinger, J.; Thomas, B.; McNabb, D. S.; Li, J. Slowing DNA Translocation in a Solid-State Nanopore. *Nano Lett.* **2005**, *5*, 1734–1737.

33. Reiner, J. E.; Robertson, J. W. F.; Burden, D. L.; Burden, L. K.; Balijepalli, A.; Kasianowicz, J. J. Temperature Sculpting in Yoctoliter Volumes. *J. Am. Chem. Soc.* **2013**, *135*, 3087–3094.

34. Levis, R. A.; Rae, J. L. The Use of Quartz Patch Pipettes for Low Noise Single Channel Recording. *Biophys. J.* **1993**, *65*, 1666–1677.

35. Dekker, R. M. M. S.; D, N. H.; C Low-Frequency Noise in Solid-State Nanopores. *Nanotechnology* **2009**, *20*, 95501.

36. Smeets, R. M.; Keyser, U. F.; Dekker, N. H.; Dekker, C. Noise in Solid-State Nanopores. *Proc. Natl. Acad. Sci. U.S.A.* **2008**, *105*, 417–421.

37. Hooge, F. N. 1/f Noise Is No Surface Effect. *Phys. Lett. A* **1969**, *29*, 139–140.

38. Smeets, R. M.; Keyser, U. F.; Wu, M. Y.; Dekker, N. H.; Dekker, C. Nanobubbles in Solid-State Nanopores. *Phys. Rev. Lett.* **2006**, *97*, 088101.

39. Chen, P.; Mitsui, T.; Farmer, D. B.; Golovchenko, J.; Gordon, R. G.; Branton, D. Atomic Layer Deposition to Fine-Tune the Surface Properties and Diameters of Fabricated Nanopores. *Nano Lett.* **2004**, *4*, 1333–1337.

40. Larkin, J.; Foquet, M.; Turner, S. W.; Korlach, J.; Wanunu, M. Reversible Positioning of Single Molecules inside Zero-Mode Waveguides. *Nano Lett.* **2014**, *14*, 6023–6029.

41. Smeets, R. M.; Keyser, U. F.; Krapf, D.; Wu, M. Y.; Dekker, N. H.; Dekker, C. Salt Dependence of Ion Transport and DNA Translocation through Solid-State Nanopores. *Nano Lett.* **2006**, *6*, 89–95.

42. Kraus, J. D. *Electromagnetics*; Carver, K. R., Ed.; McGraw-Hill Electrical and Electronic Engineering Series; McGraw-Hill: New York, 1973.

43. Zhu, P.; Craighead, H. G. Zero-Mode Waveguides for Single-Molecule Analysis. *Annu. Rev. Biophys.* **2012**, *41*, 269–293.

44. Aksimentiev, A.; Heng, J. B.; Timp, G.; Schulten, K. Microscopic Kinetics of DNA Translocation through Synthetic Nanopores. *Biophys. J.* **2004**, *87*, 2086–2097.

45. Heng, J. B.; Ho, C.; Kim, T.; Timp, R.; Aksimentiev, A.; Grinkova, Y. V.; Sligar, S.; Schulten, K.; Timp, G. Sizing DNA Using a Nanometer−Diameter Pore. *Biophys. J.* **2004**, *87*, 2905–2911.

46. Liu, H.; Qian, S.; Bau, H. H. The Effect of Translocating Cylindrical Particles on the Ionic Current through a Nanopore. *Biophys. J.* **2014**, *92*, 1164–1177.

47. Menestrina, J.; Yang, C.; Schiel, M.; Vlassiouk, I.; Siwy, Z. S. Charged Particles Modulate Local Ionic Concentrations and Cause Formation of Positive Peaks in Resistive-Pulse-Based Detection. *J. Phys. Chem. C* **2014**, *118*, 2391–2398.

48. Ling, D. Y.; Ling, X. S. On the Distribution of DNA Translocation Times in Solid-State Nanopores: An Analysis Using Schrödinger's First-Passage-Time Theory. *J. Phys.: Condens. Matter* **2013**, *25*, 375102.

49. Venta, K.; Shemer, G.; Puster, M.; Rodríguez-Manzo, J. A.; Balan, A.; Rosenstein, J. K.; Shepard, K.; Drndić, M. Differentiation of Short, Single-Stranded DNA Homopolymers in Solid-State Nanopores. *ACS Nano* **2013**, *7*, 4629–4636.

50. Ivankin, A.; Henley, R. Y.; Larkin, J.; Carson, S.; Toscano, M. L.; Wanunu, M. Label-Free Optical Detection of Biomolecular Translocation through Nanopore Arrays. *ACS Nano* **2014**, *8*, 10774–10781.

51. Jonsson, M. P.; Dekker, C. Plasmonic Nanopore for Electrical Profiling of Optical Intensity Landscapes. **2013**, 8−12.

52. Jothimuthu, P.; Carroll, A.; Bhagat, A. A. S.; Lin, G.; Mark, J. E.; Papautsky, I. Photodefinable PDMS Thin Films for Microfabrication Applications. *J. Micromech. Microeng.* **2009**, *19*, 45024.

53. Eilers, P. H. C.; Boelens, H. F. M. *Baseline Correction with Asymmetric Least Squares Smoothing*; Leiden University Medical Centre: Leiden, The Netherlands, **2005**.

54. Srisa-Art, M.; deMello, A. J.; Edel, J. B. Fluorescence Lifetime Imaging of Mixing Dynamics in Continuous-Flow Microdroplet Reactors. *Phys. Rev. Lett.* **2008**, *101*, 14502.

55. i Solvas, X. C.; Srisa-Art, M.; deMello, A. J.; Edel, J. Mapping of Fluidic Mixing in Microdroplets with 1 μs Time Resolution Using Fluorescence Lifetime Imaging. *Anal. Chem.* **2010**, *82*, 3950–3956.